

Probing type-II Ising pairing using the spin-mixing parameter

Paulina Jureczko,¹ Jozef Haniš,² Paulo E. Faria Junior,³ Martin Gmitra,^{2,4,*} and Marcin Kurpas^{5,†}

¹*Institute of Physics, University of Silesia in Katowice, 41-500 Chorzów, Poland*

²*Institute of Physics, Pavol Jozef Šafárik University in Košice, Park Angelinum 9, 04001 Košice, Slovakia*

³*Institute for Theoretical Physics, University of Regensburg, 93040 Regensburg, Germany*

⁴*Institute of Experimental Physics, Slovak Academy of Sciences, Watsonova 47, 04001 Košice, Slovakia*

⁵*Institute of Physics, University of Silesia in Katowice, 41-500 Chorzów, Poland*

(Dated: March 27, 2024)

The immunity of Ising superconductors to external magnetic fields originates from a spin locking of the paired electrons to an intrinsic Zeeman-like field. The spin-momentum locking in non-centrosymmetric crystalline materials leads to type-I Ising pairing in which the direction of the intrinsic field can be deduced from the spin expectation values. Conversely, in centrosymmetric crystals the electron spins locked to the orbitals can form Ising type-II pairs consisting of spin-orbit split doublets. Due to time-reversal symmetry, the doublets are spin degenerate, making it difficult to read the spin polarization of bands and the direction of spin-orbit fields. Here we present an efficient approach to determine the direction of the intrinsic field using the spin-mixing parameter b^2 . Using first principles calculations based on the density functional theory, we study monolayer transition metal dichalcogenide superconductors PdTe₂, NbTe₂, and TiSe₂ with the 1T structure. We calculate b^2 for individual Fermi pockets and provide a general picture of possible Ising type-II pairing within the full Brillouin zone. In order to complement our first principles results, we use group theory to provide a detailed picture of spin-orbit coupling and spin mixing in the relevant bands forming Fermi pockets. We demonstrate that contrary to the anticipated effects of spin-orbit locking, not every spin-orbit split spin doublet actively participates in Ising pairing. Finally, by connecting the spin-mixing parameter b^2 with the intrinsic out-of-plane Zeeman field we estimate the upper in-plane critical magnetic field.

I. INTRODUCTION

Quantum confinement in thin superconductors significantly eliminates orbital effects for an in-plane magnetic field leading to the enhancement of the upper critical fields [1]. Superconductivity has recently moved from thin films to crystalline atomically thin systems [2, 3] conducting fascinating quantum phenomena. A recent breakthrough was the discovery of unconventional Ising pairing responsible for extremely large magnetic in-plane upper critical fields [4, 5]. The Ising type-I superconducting pairing has been first identified in ionic-gated MoS₂ [2, 6] and further confirmed in NbSe₂ [7, 8] and in other trigonal prismatic polytypes transition metal dichalcogenides (TMDC) [8–13]. An unconventional superconducting behavior has been also reported in 1T'-MoS₂ [14] and in few-layer stanene [15] suggesting the Ising type-II pairing [16].

Spin-orbit coupling (SOC) combines orbital crystal symmetry and spin effects impacting the spin degeneracy of the electronic bands [17, 18]. For crystals with broken inversion symmetry, SOC leads to spin splitting of the electronic bands except for the time-reversal invariant points, while the band spin degeneracy is preserved in the centrosymmetric crystals. In the former case, the Fermi surface splits into two sheets with different densities of states at the Fermi level and independent super-

conducting pairing. SOC can also lead to the mixing of singlet and triplet pairing [19, 20] and to the enhancement of upper critical field in topological superconductors with space inversion symmetry [21, 22]. It is thus an important ingredient for the emergence of unconventional electron pairing [23] in crystalline systems.

Based on the general band spin splitting, we distinguish two types of Ising superconductors in two-dimensional (2D) materials. The Ising type-I superconductors [6], such as 1H polytype NbSe₂ or MoSe₂, have broken inversion symmetry but possess a horizontal mirror plane σ_h which protects the spins in the perpendicular direction due to a strong SOC field B_{so} , also called an intrinsic Zeeman field. A giant in-plane upper critical magnetic field $B_{||}$ is needed to compensate for the protecting B_{so} [2, 7, 11]. The robustness of the Ising pairing can be approximately estimated by comparing the spin splitting of the relevant bands close to the Fermi level, $2\Delta_{so} = \mu_B B_{so}$ with the Zeeman spin splitting Δ_Z due to an external magnetic field $B_{||}$. The ratio $B_{eff,||} = B_{||}^2/B_{so}$, defines an effective in-plane component of the magnetic field. When $B_{eff,||}$ reaches the Pauli paramagnetic limit $B_{eff,||} \sim B_P \approx 1.84 T_c$ [24, 25], the Cooper pair breaking takes place destroying the superconducting condensate [7]. From this condition, the upper critical field $B_{c2,||}$ at $T = 0K$ can be estimated as $B_{c2,||} \approx \sqrt{B_{so} B_P}$. For typical Zeeman splitting energy $\Delta_Z \approx 0.1 \text{ meV/T}$ (assuming $g_s \approx 2$), the values of $B_{c2,||}$ in 2D TMDC superconductors can reach tens of Tesla, greatly exceeding B_P [2, 6, 7, 11, 26].

Interestingly, Ising type-II superconductors can be re-

* martin.gmitra@upjs.sk

† marcin.kurpas@us.edu.pl

alized in centrosymmetric 2D materials with multiple degenerate orbitals [27]. SOC field in those systems can induce spin-orbital locking contrary to the spin-momentum locking in type-I superconductors. But similarly, an induced intrinsic out-of-plane Zeeman-like field B_{so} is insensitive to an in-plane magnetic field leading to a robust upper critical magnetic field [14–16, 28]. In centrosymmetric systems, for instance in 2D TMDCs with D_{3d} point group symmetry [27, 28], SOC splits all orbital states with orbital quantum number $\ell > 0$ and gives rise to spin degenerate doublets at the Γ point. Energy splitting of the doublets is proportional to the effective Zeeman field $B_{so}\tau_z$, where $\tau_z = \pm 1$ labels, e. g., for $\ell = 1$, $p_x \pm ip_y$ orbitals. The opposite signs of the field are related with the $p_x \pm ip_y$ orbitals. The presence of a C_3 rotation axis ensures the out-of-plane direction of the effective Zeeman field correspondingly polarizing the electron spins. To determine the spin orientation within the spin degenerate bands one can break time-reversal symmetry by applying an effective Zeeman field, and compare its effect on band spin splitting without SOC, and with SOC split doublets [27]. This approach has been applied to identify a set of type-II Ising superconductor candidates investigating states close to the center of the Brillouin zone [27].

In this paper, we propose an alternative technique to determine the direction of the intrinsic Zeeman-like field in centrosymmetric systems which do not require breaking of inversion or time reversal symmetry. The proposed technique is fully ab initio and does not require auxiliary effective models. The intrinsic Zeeman field direction is associated with the spin-mixing parameter b^2 reflecting spin-orbital locking and other features of SOC in a material. By calculating the b^2 for different spin quantization axes we determine its anisotropy and conclude on the orientation of the intrinsic SOC field and spin polarization of degenerate bands.

We test the proposed method using first principles calculations applied to three centrosymmetric 1T-polytype monolayer TMDCs classified as potential type-II Ising superconductors [27]: PdTe₂, NbTe₂, TiSe₂. Our results confirm a strong Ising pairing in PdTe₂, with the in-plane upper critical fields $B_{c2,\parallel}(T)$ up to 10 Tesla, in a perfect agreement with a recent experimental study [28]. Monolayer TiSe₂, besides significant out-of-plane spin polarization of bands around the Brillouin Zone center, is characterized by much weaker $B_{c2,\parallel}(T)$, while for NbTe₂ the almost isotropic b^2 suggests no type-II Ising superconductivity.

The proposed method is very versatile, can be easily implemented in numerical codes, and its application is not restricted only to 2D systems. It can be used to extend high-throughput screening calculations [27] of 2D Ising type-II superconductors and can give an insight into SOC contribution to the critical field anisotropy in bulk superconductors.

II. METHODS

A. Theoretical background

Our approach is based on the fundamental property, that in centrosymmetric systems, the two spin degenerate Bloch states with crystal momentum \mathbf{k} ,

$$\begin{aligned}\psi_{\mathbf{k},s}^{\uparrow}(\mathbf{r}) &= [a_{\mathbf{k},s}(\mathbf{r})\chi_s^{\uparrow} + b_{\mathbf{k},s}(\mathbf{r})\chi_s^{\downarrow}] \exp(i\mathbf{k} \cdot \mathbf{r}), \\ \psi_{\mathbf{k},s}^{\downarrow}(\mathbf{r}) &= [a_{-\mathbf{k}}^*(\mathbf{r})\chi_s^{\downarrow} - b_{-\mathbf{k}}^*(\mathbf{r})\chi_s^{\uparrow}] \exp(i\mathbf{k} \cdot \mathbf{r}),\end{aligned}\quad (1)$$

are mixtures of spin *up* and *down* states, χ_s^{\uparrow} and χ_s^{\downarrow} , respectively. Here, $a_{\mathbf{k},s}(\mathbf{r})$ and $b_{\mathbf{k},s}(\mathbf{r})$ are lattice periodic functions, and s stands for the spin quantization axis (SQA), $s = \{x, y, z\}$.

The states χ_s^{σ} are eigenstates of spin one-half operator \hat{s} , whose choice depends on the SQA. For instance, for SQA along the x axis ($s = x$), χ_s^{σ} diagonalize the \hat{s}_x Pauli spin matrix.

In the above Bloch states, the *admixture coefficient* $b_{\mathbf{k},s}(\mathbf{r})$ is the amplitude of the spin component admixed by SOC to a pure spin state and vanishes if SOC is absent [18]. The spin mixing parameter $b_{\mathbf{k},s}^2$ is defined as the integral of $b_{\mathbf{k},s}(\mathbf{r})$ over the whole unit cell

$$b_{\mathbf{k},s}^2 = \int_{V_{\text{cell}}} |b_{\mathbf{k},s}(\mathbf{r})|^2 d\mathbf{r}. \quad (2)$$

For spin one-half particles, $b_{\mathbf{k},s}^2$ can be also expressed as a deviation of spin expectation value from its nominal value 1/2 (in units of \hbar):

$$b_{\mathbf{k},s}^2 = 1/2 - |\langle \psi_{\mathbf{k},s}^{\sigma} | \hat{s} | \psi_{\mathbf{k},s}^{\sigma} \rangle|, \quad (3)$$

where $\sigma = \{\uparrow, \downarrow\}$ and \hat{s} is the spin one-half operator diagonal in the basis given by the choice of the SQA [29]. For normalized states $b_{\mathbf{k},s}^2$ varies from 0 for pure spinors to 0.5 for maximally spin mixed states. Usually, it takes a small value due to a weakness of SOC but can be greatly enhanced at special points of the Brillouin zone, such as high symmetry points, accidental degeneracies or BZ edges, leading to a strong spin mixing [30]. A more comprehensive discussion of the spin mixing parameter can be found in Refs. [29–32].

The value of $b_{\mathbf{k},s}^2$ characterizes the strength of the spin-orbit interaction in a band, while its anisotropy for SQAs reflects the anisotropy of SOC and describes the preferred direction of the intrinsic SOC fields (Zeeman-like field) and spin polarization [29]. Thus, calculating $b_{\mathbf{k},s}^2$ and its anisotropy for individual Fermi pockets should infer their potential contribution to the Ising pairing.

B. Details of first principles calculations

The monolayers of the 1T-polytypes of TMDC are derived from the bulk variants crystallizing in space group 164 with metal atoms (Pd, Nb, Ti) in Wyckoff position 1a

(0,0,0), and the chalcogen atoms (Se,Te) in 2d positions (2/3, 1/3, d). We considered vacuum spacing of 20 Å to eliminate periodic images in the vertical direction.

The first principles calculations were performed using the open source code suite QUANTUM ESPRESSO [33, 34], implementing pseudopotential and plane wave approaches to the density functional theory. We used scalar and fully relativistic SG15 Optimized Norm-Conserving Vanderbilt (ONCV) pseudopotentials [35, 36]. The kinetic energy cutoffs for the wave function were 52 Ry, 53 Ry, 52 Ry for PdTe₂, NbTe₂, and TiSe₂ respectively, while cutoffs for the charge density were four times bigger. These values were sufficient to obtain well-converged values of orbital and spin-related quantities.

The lattice parameters and atomic positions in the unit cell were optimized to minimize strain and internal forces. The lattice constants were determined by finding the minimum of a quadratic function fitted to the first principles data of total energy calculated for several values of a . Later, the positions of atoms were fully relaxed using the quasi-Newton scheme as implemented in QUANTUM ESPRESSO package. The optimized lattice constants and vertical positions of the chalcogen atoms are $a = 4.02$ Å, $d = 1.4$ Å for PdTe₂, $a = 3.67$ Å, $d = 1.86$ Å for NbTe₂, and $a = 3.54$ Å, $d = 1.55$ Å for TiSe₂, and agrees well with the experimental values; for PdTe₂, TiSe₂ in monolayer [28, 37] and for NbTe₂ in ultrathin nanoplates [38]. Self-consistency was obtained with $21 \times 21 \times 1$ Monkhorst-Pack grid sampling of the first Brillouin zone (BZ). The Fermi contour averages of the spin-mixing parameter b^2 were calculated using the tetrahedron method with an adaptive mesh of k -points according to the formula

$$b_s^2 \equiv \langle b_{\mathbf{k},s}^2 \rangle_{\text{FC}} = \frac{1}{\rho(E_F)S_{\text{BZ}}} \int_{\text{FC}} \frac{b_{\mathbf{k},s}^2}{\hbar|\mathbf{v}_F(\mathbf{k})|} d^2k, \quad (4)$$

where S_{BZ} is the area of the Fermi surface within the first Brillouin zone, FC stands for Fermi contour, $\rho(E_F)$ is the density of states per spin at the Fermi level, and $\mathbf{v}_F(\mathbf{k})$ is the Fermi velocity. The mesh density was iteratively increased, using as a criterion variation of $b_{\mathbf{k}}^2$, until convergence of the average b^2 has been reached. The number of generated k -points in each Fermi pocket varied between 2000 and 5000.

III. RESULTS

A. First principles calculations

In this section, we present the results of our first principles calculations. First, we discuss PdTe₂. Among all materials studied here, it is the only one for which the in-plane upper critical field has been measured [28]. Therefore it represents a platform to test the proposed approach. We mention that PdTe₂ crystal is topologically non-trivial material and host Dirac type-II Fermions [39, 40]. It becomes a superconductor around $T_c = 1.7$ K

[41]. Recent measurements on a few-layer PdTe₂ sample have shown, that the Pauli limit for the critical magnetic field is of $B_P \approx 1.29$ T for 4-layer and $B_P \approx 1.36$ T for 6-layer thick samples exceeded 7 times the Pauli limit corroborating the Ising type-II pairing [28].

In Fig. 1(b) we show the calculated orbital resolved relativistic band structure of monolayer PdTe₂. In this energy range, the bands of PdTe₂ are formed mainly by the p -electrons of tellurium with a small admixture of Pd d -electrons the band B_2 and bands of higher energy. In the vicinity of the Γ point, the band B_1 that crosses the Fermi energy is a linear combination of p_x and p_y Te electrons, up to the anticrossing at the energy around -0.5 eV, when the contribution from p_z electrons starts to be visible (see also Fig. S2 in the Supplemental Material [42]).

Recent explanation of the Ising type-II pairing [16, 27, 43] involves the spin-orbit split-off orbital doublet ($p_x \pm ip_y, \sigma$) around the Γ point. For PdTe₂

the orbital doublet is formed by the band B_1 with the total angular momentum $J_z = 3/2$ and the band B_3 with $J_z = 1/2$, which without SOC are four-fold degenerate at the Γ point see Fig. S1(a) in the Supplemental Material [42]. The split-off energy is proportional to the SOC strength and is a direct measure of the spin-orbit locking of the spins in out-of-plane direction [28]. The band resolved calculation of the b^2 for the B_1 band, see Fig. 1(c), reveals a suppression of the b^2 parameter for the SQA along the z direction in comparison to the in-plane directions. For the latter, $b^2 \approx 0.5$, which happens when $|a_{\mathbf{k},x/y}(\mathbf{r})| \approx |b_{\mathbf{k},x/y}(\mathbf{r})|$, and the spin expectation values for the in-plane components $|\langle \psi_{\mathbf{k},x/y}^\sigma | \hat{s}_{x/y} | \psi_{\mathbf{k},x/y}^\sigma \rangle| \approx 0$ [29], which clearly demonstrates the out-of-plane polarization of spins and the intrinsic SOC field.

It is convenient to express the anisotropy of the spin mixing parameter b^2 by the polarization P in the following form

$$P = \frac{b_{\parallel}^2 - b_{\perp}^2}{b_{\parallel}^2 + b_{\perp}^2}, \quad (5)$$

where $b_{\parallel}^2 = (b_x^2 + b_y^2)/2$ and $b_{\perp}^2 = b_z^2$. The polarization is valued $-1 \leq P \leq 1$ from in-plane to out-of-plane direction, while for $P = 0$ no anisotropy is expected. From the above definition, it is clear, that Ising pairing is effective only when P is close to one.

In Fig. 2(b) we show P calculated for the B_1 band of PdTe₂ versus doping up to the edge of this band at the Γ point. The strong out-of-plane spin polarization, $P \approx 1$, supports the observed Ising type-II pairing in this case [28].

The band B_2 forms two pockets along ΓK and ΓM lines with a mixture of all Te p electrons and a small admixture of Pd d -electrons at the vicinity of the Fermi level (Fig. 1(b) and Fig. S2 in the Supplemental Material [42]). The calculated b^2 for both the pockets shows almost equal amplitudes for all the SQA components, see Fig. 1(d) and Fig. 1(e), which leads to small anisotropy

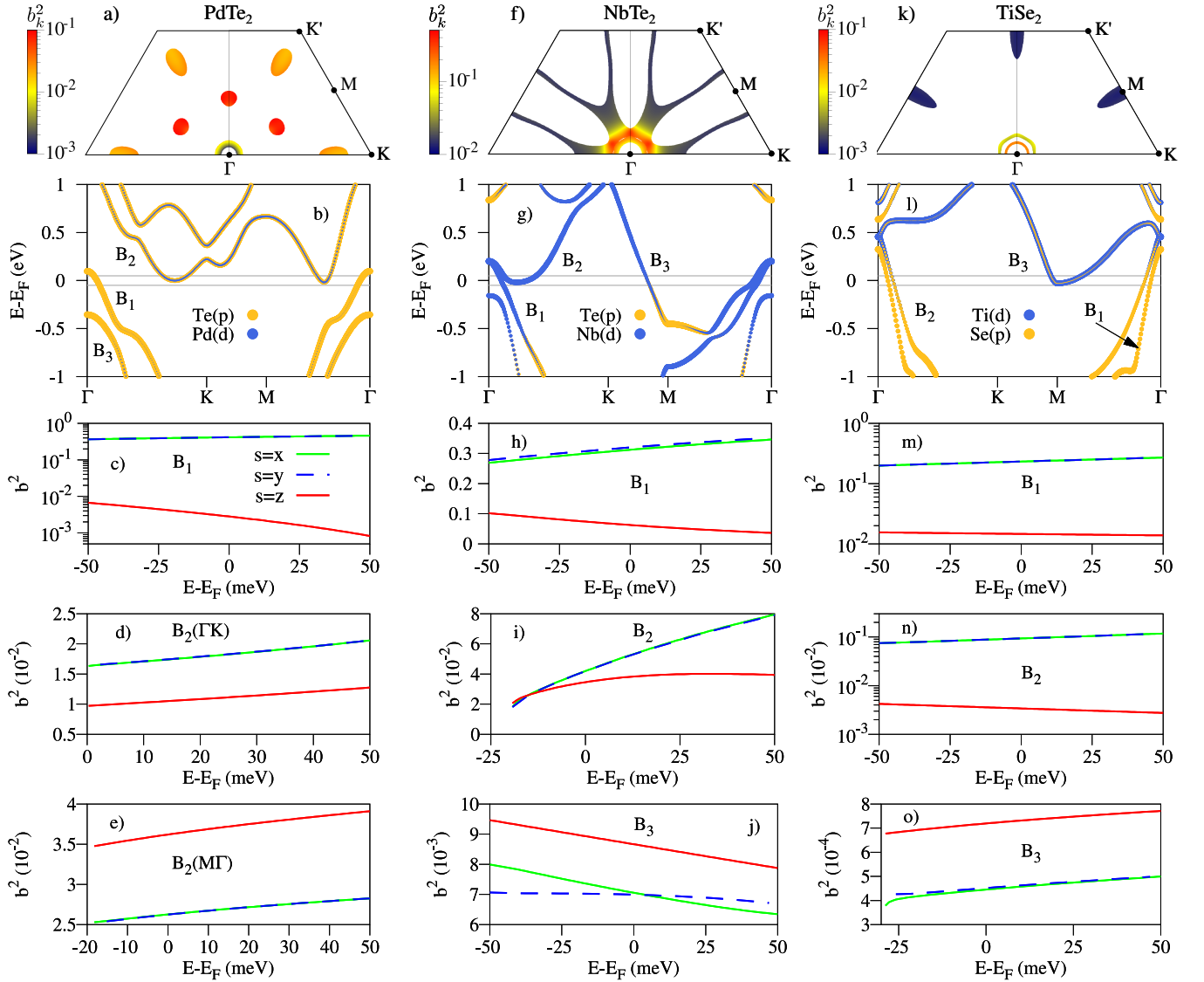


FIG. 1. Calculated orbital and spin-orbital properties of 1T-polytype monolayers of transition metal dichalcogenides. (a) band pockets in energy window ± 50 meV around the Fermi energy for PdTe₂ in the Brillouin zone wedge. The colormap corresponds to b_k^2 for SQA $s = z$. (b) orbital resolved band structures of PdTe₂ with the indicated bands crossing the Fermi energy. Grey horizontal lines depict the ± 50 meV energy window around the Fermi energy for which the average spin-mixing parameter b^2 was calculated. (c), (d), (e) Fermi contour averaged spin-mixing parameter b^2 calculated for the Fermi pockets formed by the bands B_1 and B_2 depicted in (a) for three spin quantization axes $s = \{x, y, z\}$ aligned with the Cartesian axes. Similarly, the middle and right row for NbTe₂ and TiSe₂.

of b^2 . The polarization P for the pocket along the ΓK line is $P \approx 0.23$ and for the pocket along the ΓM line $P \approx -0.17$, which indicates that Ising pairing in the band B_2 is ineffective. This result is consistent with the common interpretation that type-II Ising superconductivity requires multiple degenerate bands.

The large polarization for the B_1 band suggests that a hole doping of the PdTe₂ should eliminate the B_2 pockets and provide enhancement of the Ising type-II pairing due to large b^2 anisotropy. For heavy hole doping due to the presence of a substrate the B_3 band being the orbital doublet partner of the band B_1 , may potentially

give rise to the Ising pairing. The calculated spin-mixing parameter b^2 and polarization P show, however, that the Ising mechanism is not present in the band B_3 due to the dominant in-plane direction of spin-orbit fields and weak anisotropy, see Fig. S3 in the Supplemental Material [42]. We explain the weak anisotropy in this band in the Sec. III B.

Superconductivity in niobium dichalcogenides down to monolayer limit has been extensively studied [7, 11, 44–47]. NbTe₂ is a polytypic TMDC exhibiting peculiar 1T distortions and pressure-induced phase transitions [48]. Recently cathodic exfoliation of NbTe₂ shows a trigo-

nal structure of the flakes [49]. NbTe₂ belongs to the group 5 TMDCs nominally having one *d*-electron and is metallic [50]. The superconducting temperature was reported at $T_c = 0.5\text{--}0.72\text{ K}$ [45, 51, 52]. In Fig. 1(f) we plot b_k^2 in the Brillouin zone wedge within the pockets for energies $\pm 50\text{ meV}$ around the Fermi level. The corresponding averaged b^2 dependencies for the indicated bands in Fig. 1(g) are plotted in Fig. 1(h-j). The Bloch states near the Fermi level are predominantly formed by the *d*-orbitals of Nb atoms. The band resolved averaged b^2 indicates a rather small anisotropy, thus leading to reduced polarization values, $|P| \in [0, 0.75]$.

Due to this small anisotropy of b^2 , we speculate that the NbTe₂ is not a good candidate to be a type-II Ising superconductor.

Two-dimensional TiSe₂ has been extensively studied to probe the interplay between superconductivity and possible charge-density waves via doping [53–56], intercalation [57–61], pressure [62, 63], and layer thickness [64, 65]. The charge-density wave phase can be suppressed by intercalation [55, 60] or pressure [62], and superconducting critical temperature ranges $T_c = 0.7\text{--}3.9\text{ K}$ [59]. The calculated b_k^2 is shown in Fig. 1(k) for the Fermi pockets within the energy window $\pm 50\text{ meV}$ formed by the three bands, B_1 and B_2 around the Γ point, and B_3 around the M point. The orbital resolved band structure of TiSe₂ shown in Fig. 1(l) reveals that the states near the M points are formed by the Ti *d*-orbitals. The remaining bands are formed by the *p*-orbitals of Se atoms, and *d*-orbitals of Ti in the case of the band B_2 , see Fig. S4 in the Supplemental Material [42]. The band resolved spin-mixing parameters for the B_1 and B_2 bands, see Fig. 1(m,n) exhibit distinct but smaller anisotropy than B_1 of PdTe₂, within the whole doping range, $b_{\parallel}^2/b_{\perp}^2 \approx 10\text{--}30$. The values of P vary between 0.85 and 0.9 for the B_1 band and between 0.9 and 0.95 for the B_2 band, see Fig. S6 in the Supplemental Material [42]. In comparison, for the B_3 band $b_{\parallel}^2/b_{\perp}^2 \approx 2$, see Fig. 1(o). Thus, one can expect that only bands B_1 and B_2 will give a relevant contribution to the Ising enhancement of the upper critical fields in TiSe₂.

B. The origin of spin mixing

To understand the mechanism of spin mixing in the studied materials, we analyze the spin-orbit coupling in the band structure using symmetry arguments, following Refs. [32, 66]. We discuss in detail PdTe₂ here in the main text, and the analogous analysis for NbTe₂ and TiSe₂ can be found in the Supplemental Material [42].

The bands relevant for Ising pairing are B_1 and B_3 close to the Γ point. Without SOC these bands are degenerate and transform as the Γ_3^- irrep of the D_{3d} point group, see Fig. S1(a) in the Supplemental Material [42]. The intraband SOC leads to the Hamiltonian

$$H_{\text{intra}} = -\Delta_z s_z \sigma_y, \quad (6)$$

in the basis $\{|\Gamma_{3,1}^- \uparrow\rangle, |\Gamma_{3,2}^- \uparrow\rangle, |\Gamma_{3,1}^- \downarrow\rangle, |\Gamma_{3,2}^- \downarrow\rangle\}$ with $\Gamma_{3,1}^- \sim x$ and $\Gamma_{3,2}^- \sim y$, Δ_z is the SOC strength, s_z is spin one-half operator and σ_y is the Pauli matrix in y direction acting in the orbital subspace. The Hamiltonian (6) splits off the bands by $2|\Delta_z|$, but leaves the spin unchanged, giving no spin mixing ($b^2 = 0$). The eigenstates of H_{intra} are pure s_z spinors, $|\Gamma_{3\pm}^- \sigma\rangle = \frac{1}{\sqrt{2}} (|\Gamma_{3,1}^- \rangle \pm i |\Gamma_{3,2}^- \rangle) |\sigma\rangle$, $\sigma = \{\uparrow, \downarrow\}$, due to time-reversal symmetry which does not allow spin-flip terms in (6). Mixing of spins originates from the interband SOC, for which no such restriction applies. Treating SOC perturbatively (see the Supplemental Material [42] for details) we get new wave functions of the SOC split doublets B_1 and B_3

$$\begin{aligned} |\Gamma_{3+}^- \uparrow\rangle_{B_1} &= |\Gamma_{3+}^- \uparrow\rangle + \alpha |\beta \uparrow\rangle + \gamma |\beta \downarrow\rangle, \\ |\Gamma_{3-}^- \downarrow\rangle_{B_1} &= |\Gamma_{3-}^- \downarrow\rangle + \alpha |\beta \downarrow\rangle + \gamma |\beta \uparrow\rangle, \\ |\Gamma_{3+}^- \downarrow\rangle_{B_3} &= |\Gamma_{3+}^- \downarrow\rangle + \delta |\beta \downarrow\rangle + \zeta |\beta \uparrow\rangle, \\ |\Gamma_{3-}^- \uparrow\rangle_{B_3} &= |\Gamma_{3-}^- \uparrow\rangle + \delta |\beta \uparrow\rangle + \zeta |\beta \downarrow\rangle, \end{aligned} \quad (7)$$

where $\alpha, \gamma, \delta, \zeta$ are complex coefficients. It is clear, that the states (7) are mixtures of spin *up* and spin *down* components giving $b^2 \neq 0$. Different coefficients in the states (7) indicate different spin mixing in the bands B_1 and B_3 . Indeed, our theoretical analysis reveals that spin mixing in the band B_1 results from the coupling of the Γ_3^- band to other Γ_3^- bands, while in B_3 it comes from the coupling to the bands with Γ_1^- and Γ_2^- irreducible representations. In PdTe₂ the closest Γ_3^- band lies 6.5 eV above the relevant Γ_3^- band, and the intraband SOC dominates over the weak interband coupling, which explains the small value of b_z^2 and large anisotropy of spin mixing. The weak anisotropy of b^2 in the band B_3 is a common effect of the intraband spin-conserving SOC and the interband spin-flip coupling between the Γ_3^- and the nearby Γ_2^- band (see Fig. 3(a) in the Supplemental Material [42]).

According to the recent interpretation of the Ising pairing mechanism involving degenerate orbitals, due to spin-orbit locking the spin-orbit split doublets, such as B_1 and B_3 in PdTe₂, should display a perfect out-of-plane spin polarization [16, 28]. Our numerical results for b^2 supported by symmetry analysis show, that such a picture is simplified. The doublet partner bands exhibit considerably different spin polarization direction due to coupling to different bands via SOC. The spin mixing parameter b^2 detects these differences, which proves the reliability of the proposed method in detecting Fermi contours relevant for possible Ising pairing.

C. Estimation of the upper critical field $B_{c2,\parallel}$

To stress the experimental relevance of our method we will now estimate the upper critical field B_{c2} for PdTe₂. Monolayer PdTe₂ crystallizes in $P3\bar{m}1$ space group being isomorphic with D_{3d} point group. At the Brillouin zone center, the presence of the C_3 rotation axis forbids the in-plane spin components and ensures the out-of-plane orientation of the intrinsic SOC field.

Away from the Γ point, such restriction is released and all components of the intrinsic Zeeman field \mathbf{B} are allowed, $\mathbf{B} = (B_x, B_y, B_z)$. Next, we make an assumption, that the main contribution to the splitting of the bands B_1 and B_3 comes from the intraband SOC, while the interband SOC Hamiltonian contributes mainly to spin expectation values and spin mixing. This assumption is reliable as long as $b_z^2 \approx 0 \Rightarrow P \approx 1$, which also allows us to select the relevant bands that are more susceptible to host Ising pairing superconductivity. Furthermore, for bands with $b_z^2 \approx 0 \Rightarrow P \approx 1$, a g-factor of ≈ 2 is expected, since they would share nearly the same orbital character with opposite spins [67]. With this picture in mind, the splitting energy can be written as $\Delta_{\text{so}} = 2|\Delta_z| = g_s \mu_B B$, where $B = \|\mathbf{B}\| = \sqrt{B_x^2 + B_y^2 + B_z^2}$, and $g_s = 2$, is the electron Lande factor. We are interested in the in-plane to out-of-plane anisotropy, thus it is convenient to rewrite Δ_{so} as $\Delta_{\text{so}} = 2\mu_B \sqrt{B_{\parallel}^2 + B_{\perp}^2}$, where $B_{\parallel} = \sqrt{B_x^2 + B_y^2}$ and $B_{\perp} = B_z$. We can now relate the direction of \mathbf{B} to the polarization vector P

$$B_{\parallel} = \frac{B}{\sqrt{2\sqrt{1+P^2}}} (1-P), \quad (8)$$

$$B_{\perp} = \frac{B}{\sqrt{2\sqrt{1+P^2}}} (1+P). \quad (9)$$

Since the Ising pairing is most effective when $B_{\parallel} \approx 0$ and $B_{\perp} \approx 1$ (or $P \approx 1$) we can consider only B_{\perp} . Replacing B in (8) with $\Delta_{\text{so}}/2\mu_B$ gives

$$B_{\perp} = \frac{\Delta_{\text{so}}}{2\mu_B} \frac{1}{\sqrt{2\sqrt{1+P^2}}} (1+P), \quad (10)$$

where P and Δ_{so} are extracted from our first principles calculations. Away from the Γ point Δ_{so} at a given \mathbf{k} -point is calculated using the formula

$$\Delta_{\text{so}} = \Delta_{n,m}^{\text{rela}} - \Delta_{n,m}^{\text{nrel}}, \quad (11)$$

where $\Delta_{n,m}^{\text{rela/nrel}} = E_m - E_n$ is the energy distance between the bands n and m forming the spin-orbit split doublets, and superscript refers to relativistic/non-relativistic calculations, i. e., calculations with and without SOC, respectively. For PdTe₂ the indices m and n correspond to the B_1 and B_3 bands, respectively.

Knowing B_{\perp} we can estimate the in-plane upper critical field $B_{c2,\parallel}$ at 0 K following Ref. [7]

$$B_{c2,\parallel} \sim \sqrt{B_P B_{\perp}}. \quad (12)$$

The results are shown in Fig. 2. Due to the large Δ_{so} and $P \approx 1$, the values of B_{\perp} are giant, on the order of 10^3 Tesla, resulting in $B_{c2,\parallel}(0 \text{ K})$ exceeding the Pauli limit by more than fifty times. The large value of B_{\perp} is mainly determined by large Δ_{so} , since in the whole range of doping $P \approx 1$.

To estimate $B_{c2,\parallel}$ at finite temperatures we use the microscopic model for the one-band Ising superconductivity

from Ref. [68], which was used in Ref. [28] to extract $B_{c2,\parallel}$ for PdTe₂. Using the same model and material parameters (see Supplemental Material [42] for details) will give us a direct comparison of our method with the experimental data.

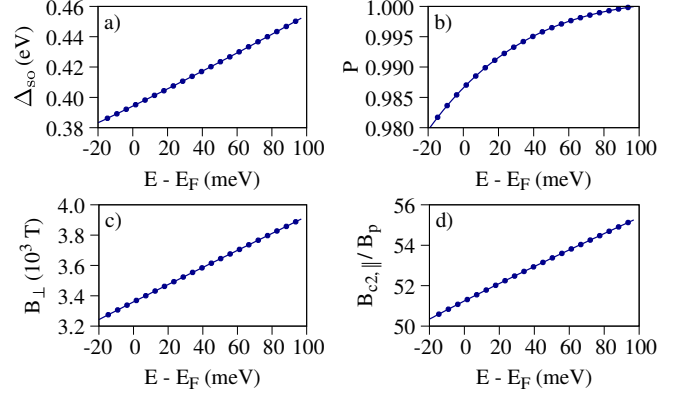


FIG. 2. Calculated properties for monolayer PdTe₂ at 0 K as a function of the Fermi energy. (a) The Fermi contour averaged spin-orbit splitting Δ_{so} , (b) polarization vector P , (c) intrinsic out-of-plane Zeeman field B_{\perp} and (d) in-plane upper critical field $B_{c2,\parallel}$ in units of Pauli field B_P .

The calculated values of the in-plane upper critical field $B_{c2,\parallel}(T)$, see Fig. 3 (a), are in very good agreement with the experimental values, taking into account small differences between the number of layers and other factors present in the experimental setup. For 6-layer PdTe₂ the experimental values of $B_{c2,\parallel}(T)$ vary from $6 B_P$ to $8 B_P$ for $T \in [0.2 \text{ K}, 0.6 \text{ K}]$ [28]. Our theoretical values for the same temperatures are slightly smaller due to momentum dependence of the spin-orbit gap Δ_{so} . Taking $\Delta_{\text{so}}(\Gamma) = 0.45 \text{ eV}$ we get $B_{c2,\parallel}(T)$ between $5 B_P$ and $10 B_P$, pointing for stronger out-of-plane spin polarization of bands. We note, that we did not use here any free or fitting parameter.

Similar analysis performed for the bands B_1 and B_2 of TiSe₂ indicates that despite relatively large Δ_{so} the values of $B_{c2,\parallel}(0 \text{ K})$ and $B_{c2,\parallel}(T)$ are considerably smaller than for PdTe₂, see (Fig. 3 (b) and Fig. S6 and Fig. S7 in the Supplemental Material [42], indicating that the Ising pairing in TiSe₂ would require relatively low temperatures and high electron doping.

IV. CONCLUSIONS

We have proposed an efficient approach to analyze the direction of intrinsic spin-orbit coupling fields and spin polarization in the band structure using the anisotropy of the spin-mixing parameter b^2 . This information is crucial for understanding the impact of type-II Ising pairing in superconductors with space inversion centers. By applying first principles calculations, we tested this approach on three monolayer transition metal dichalcogenide superconductors in the T phase: PdTe₂, NbTe₂, and TiSe₂.

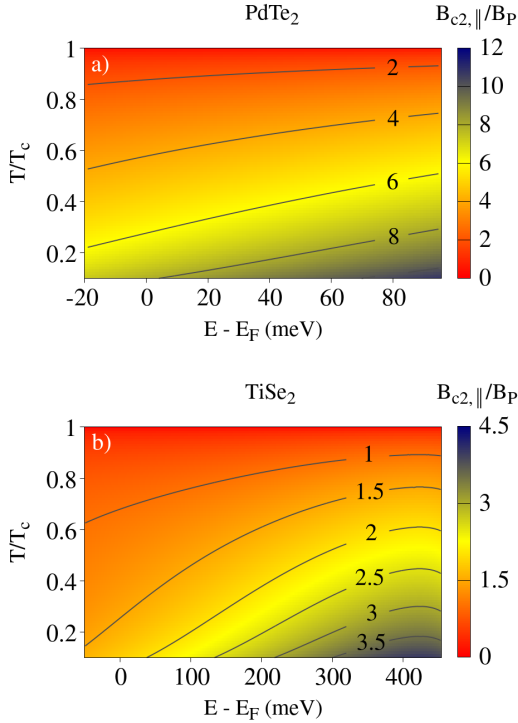


FIG. 3. The upper critical field $B_{c2,||}$ versus temperature and the Fermi level for (a) PdTe₂ and (b) TiSe₂ for band B₂ estimated using Eq. (14) from the Supplemental Material [42].

The largest anisotropy of b^2 , and the strongest expected Ising type-II pairing, is found for PdTe₂, for which our results of $B_{c2,||}$ are in excellent agreement with experimental values. Furthermore, TiSe₂ is predicted to be also a good candidate for type-II Ising superconductivity but requires considerate electron doping. In contrast to PdTe₂ and TiSe₂, we found that NbTe₂ shows a moder-

ate anisotropy of b^2 , insufficient to observe Ising pairing in this material.

The main advantage of the present approach is that it can detect possible contributions to the Ising superconductivity from individual Fermi pockets irrespective of their orbital composition and position in the Brillouin zone. As b^2 is calculated directly from the wave functions and contains all symmetry properties of the crystal, the method is very versatile and independent of the basis set. Even though we can not provide an answer to superconductivity formation in the individual Fermi pockets, by inspecting the anisotropy of b^2 one can easily select potentially relevant k momenta for type-II Ising superconductors.

ACKNOWLEDGMENTS

P.J. and M.K. acknowledge support from the Interdisciplinary Centre for Mathematical and Computational Modelling (ICM), University of Warsaw (UW), within grant no. G83-27. The project is co-financed by the Polish National Agency for Academic Exchange and by the National Center for Research and Development (NCBR) under the V4-Japan project BGapEng. J.H. and M.G. acknowledge financial support from the Slovak Research and Development Agency provided under Contract No. APVV-SK-PL-21-0055 and by the Ministry of Education, Science, Research and Sport of the Slovak Republic provided under Grant No. VEGA 1/0105/20 and Slovak Academy of Sciences project IMPULZ IM-2021-42 and project FLAG ERA JTC 2021 2DSOTECH. P.E.F.J. acknowledges the financial support of the Deutsche Forschungsgemeinschaft (DFG, German Research Foundation) SFB 1277 (Project-ID 314695032, projects B07 and B11) and SPP 2244 (Project-ID 443416183).

-
- [1] M. Tinkham, *Introduction to Superconductivity: Second Edition*, second edition ed. (Dover Publications, Mineola, NY, 2004).
 - [2] Y. Saito, Y. Nakamura, M. S. Bahramy, Y. Kohama, J. Ye, Y. Kasahara, Y. Nakagawa, M. Onga, M. Tokunaga, T. Nojima, *et al.*, Superconductivity protected by spin-valley locking in ion-gated MoS₂, *Nat. Phys.* **12**, 144 (2016).
 - [3] D. Qiu, C. Gong, S. Wang, M. Zhang, C. Yang, X. Wang, and J. Xiong, Recent Advances in 2D Superconductors, *Adv. Mater.* **33**, 2006124 (2021).
 - [4] W. Li, J. Huang, X. Li, S. Zhao, J. Lu, Z. V. Han, and H. Wang, Recent progresses in two-dimensional Ising superconductivity, *Mater. Today Phys.* **21**, 100504 (2021).
 - [5] D. Zhang and J. Falson, Ising pairing in atomically thin superconductors, *Nanotechnology* **32**, 502003 (2021).
 - [6] J. M. Lu, O. Zheliuk, I. Leermakers, N. F. Yuan, U. Zeitler, K. T. Law, and J. T. Ye, Evidence for two-dimensional Ising superconductivity in gated MoS₂, *Science* **350**, 1353 (2015).
 - [7] X. Xi, Z. Wang, W. Zhao, J. H. Park, K. T. Law, H. Berger, L. Forró, J. Shan, and K. F. Mak, Ising pairing in superconducting NbSe₂ atomic layers, *Nat. Phys.* **12**, 139 (2016).
 - [8] Y. Xing, K. Zhao, P. Shan, F. Zheng, Y. Zhang, H. Fu, Y. Liu, M. Tian, C. Xi, H. Liu, *et al.*, Ising Superconductivity and Quantum Phase Transition in Macro-Size Monolayer NbSe₂, *Nano Lett.* **17**, 6802 (2017).
 - [9] E. Navarro-Moratalla, J. O. Island, S. Mañas-Valero, E. Pinilla-Cienfuegos, A. Castellanos-Gomez, J. Qereda, G. Rubio-Bollinger, L. Chirolli, J. A. Silva-Guillén, N. Agrait, *et al.*, Enhanced superconductivity in atomically thin TaS₂, *Nat. Comm.* **7**, 11043 (2016).
 - [10] A. W. Tsen, B. Hunt, Y. D. Kim, Z. J. Yuan, S. Jia, R. J. Cava, J. Hone, P. Kim, C. R. Dean, and A. N. Pasupathy, Nature of the quantum metal in a two-dimensional crystalline superconductor, *Nat. Phys.* **12**, 208 (2016).
 - [11] S. C. De La Barrera, M. R. Sinko, D. P. Gopalan,

- N. Sivadas, K. L. Seyler, K. Watanabe, T. Taniguchi, A. W. Tsen, X. Xu, D. Xiao, and B. M. Hunt, Tuning Ising superconductivity with layer and spin-orbit coupling in two-dimensional transition-metal dichalcogenides, *Nat. Comm.* **9**, 1427 (2018).
- [12] J. Lu, O. Zheliuk, Q. Chen, I. Leermakers, N. E. Hussey, U. Zeitler, and J. Ye, Full superconducting dome of strong Ising protection in gated monolayer WS_2 , *PNAS* **115**, 3551 (2018).
- [13] Y. Tanaka, H. Matsuoka, M. Nakano, Y. Wang, S. Sasakura, K. Kobayashi, and Y. Iwasa, Superconducting $3\text{R-Ta}_{1+x}\text{Se}_2$ with Giant In-Plane Upper Critical Fields, *Nano Lett.* **20**, 1725 (2020).
- [14] J. Peng, Y. Liu, X. Luo, J. Wu, Y. Lin, Y. Guo, J. Zhao, X. Wu, C. Wu, and Y. Xie, High phase purity of large-sized $1\text{T}'\text{-MoS}_2$ monolayers with 2D superconductivity, *Adv. Mater.* **31**, 1900568 (2019).
- [15] M. Liao, Y. Zang, Z. Guan, H. Li, Y. Gong, K. Zhu, X.-P. Hu, D. Zhang, Y. Xu, Y.-Y. Wang, *et al.*, Superconductivity in few-layer stanene, *Nat. Phys.* **14**, 344 (2018).
- [16] J. Falson, Y. Xu, M. Liao, Y. Zang, K. Zhu, C. Wang, Z. Zhang, H. Liu, W. Duan, K. He, *et al.*, Type-II Ising pairing in few-layer stanene, *Science* **367**, 1454 (2020).
- [17] G. Dresselhaus, Spin-orbit coupling effects in zinc blende structures, *Phys. Rev.* **100**, 580 (1955).
- [18] R. J. Elliott, Theory of the effect of spin-orbit coupling on magnetic resonance in some semiconductors, *Phys. Rev.* **96**, 266 (1954).
- [19] L. P. Gor'kov and E. I. Rashba, Superconducting 2d system with lifted spin degeneracy: Mixed singlet-triplet state, *Phys. Rev. Lett.* **87**, 037004 (2001).
- [20] P. A. Frigeri, D. F. Agterberg, and M. Sigrist, Spin susceptibility in superconductors without inversion symmetry, *New J. Phys.* **6**, 115 (2004).
- [21] Y. M. Xie, B. T. Zhou, and K. T. Law, Spin-Orbit-Parity-Coupled Superconductivity in Topological Monolayer WTe_2 , *Phys. Rev. Lett.* **125**, 107001 (2020).
- [22] E. Zhang, Y.-M. Xie, Y. Fang, J. Zhang, X. Xu, Y.-C. Zou, P. Leng, X.-J. Gao, Y. Zhang, L. Ai, *et al.*, Spin-orbit-parity coupled superconductivity in atomically thin 2M-WS_2 , *Nat. Phys.* **19**, 106 (2023).
- [23] M. Sigrist, Introduction to Unconventional Superconductivity, *AIP Conference Proceedings* **789**, 165 (2005).
- [24] B. S. Chandrasekhar, A note on the maximum critical field of high-field superconductors, *Appl. Phys. Lett.* **1**, 7 (1962).
- [25] A. M. Clogston, Upper limit for the critical field in hard superconductors, *Phys. Rev. Lett.* **9**, 266 (1962).
- [26] Y. Saito, T. Nojima, and Y. Iwasa, Highly crystalline 2D superconductors, *Nat. Rev. Mater.* **2**, 1 (2016).
- [27] C. Wang, B. Lian, X. Guo, J. Mao, Z. Zhang, D. Zhang, B. L. Gu, Y. Xu, and W. Duan, Type-II Ising Superconductivity in Two-Dimensional Materials with Spin-Orbit Coupling, *Phys. Rev. Lett.* **123**, 126402 (2019).
- [28] Y. Liu, Y. Xu, J. Sun, C. Liu, Y. Liu, C. Wang, Z. Zhang, K. Gu, Y. Tang, C. Ding, *et al.*, Type-II Ising Superconductivity and Anomalous Metallic State in Macro-Size Ambient-Stable Ultrathin Crystalline Films, *Nano Lett.* **20**, 5728 (2020).
- [29] B. Zimmermann, P. Mavropoulos, S. Heers, N. H. Long, S. Blügel, and Y. Mokrousov, Anisotropy of Spin Relaxation in Metals, *Phys. Rev. Lett.* **109**, 236603 (2012).
- [30] J. Fabian and S. Das Sarma, Spin Relaxation of Conduction Electrons in Polyvalent Metals: Theory and a Realistic Calculation, *Phys. Rev. Lett.* **81**, 5624 (1998).
- [31] Y. Mokrousov, H. Zhang, F. Freimuth, B. Zimmermann, N. H. Long, J. Weischenberg, I. Souza, P. Mavropoulos, and S. Blügel, Anisotropy of spin relaxation and transverse transport in metals, *J. Phys.: Condens. Matter* **25**, 163201 (2013).
- [32] M. Kurpas, P. E. Faria Junior, M. Gmitra, and J. Fabian, Spin-orbit coupling in elemental two-dimensional materials, *Phys. Rev. B* **100**, 125422 (2019).
- [33] P. Giannozzi, S. Baroni, N. Bonini, M. Calandra, R. Car, C. Cavazzoni, D. Ceresoli, G. L. Chiarotti, M. Cococcioni, I. Dabo, *et al.*, QUANTUM ESPRESSO: a modular and open-source software project for quantum simulations of materials, *J. Phys.: Condens. Matter* **21**, 395502 (2009).
- [34] P. Giannozzi, O. Andreussi, T. Brumme, O. Bunau, M. B. Nardelli, M. Calandra, R. Car, C. Cavazzoni, D. Ceresoli, M. Cococcioni, *et al.*, Advanced capabilities for materials modelling with Quantum ESPRESSO, *Journal of Physics: Condensed Matter* **29**, 465901 (2017).
- [35] D. R. Hamann, Optimized norm-conserving vanderbilt pseudopotentials, *Phys. Rev. B* **88**, 085117 (2013).
- [36] P. Scherpelz, M. Govoni, I. Hamada, and G. Galli, Implementation and Validation of Fully Relativistic GW Calculations: Spin-Orbit Coupling in Molecules, Nanocrystals, and Solids, *J. Chem. Theory Comput.* **12**, 3523 (2016).
- [37] J.-P. Peng, J.-Q. Guan, H.-M. Zhang, C.-L. Song, L. Wang, K. He, Q.-K. Xue, and X.-C. Ma, Molecular beam epitaxy growth and scanning tunneling microscopy study of TiSe_2 ultrathin films, *Phys. Rev. B* **91**, 121113(R) (2015).
- [38] J. Li, B. Zhao, P. Chen, R. Wu, B. Li, Q. Xia, G. Guo, J. Luo, K. Zang, Z. Zhang, *et al.*, Synthesis of Ultrathin Metallic MTe_2 ($\text{M} = \text{V}, \text{Nb}, \text{Ta}$) Single-Crystalline Nanoplates, *Adv. Mater.* **30**, 1 (2018).
- [39] H.-J. Noh, J. Jeong, E.-J. Cho, K. Kim, B. I. Min, and B.-G. Park, Experimental realization of type-II Dirac fermions in a PdTe_2 superconductor, *Phys. Rev. Lett.* **119**, 016401 (2017).
- [40] F. Fei, X. Bo, R. Wang, B. Wu, J. Jiang, D. Fu, M. Gao, H. Zheng, Y. Chen, X. Wang, *et al.*, Nontrivial Berry phase and type-II Dirac transport in the layered material PdTe_2 , *Phys. Rev. B* **96**, 041201(R) (2017).
- [41] J. von Guggenheim, F. Hulliger, and J. Müller, PdTe_2 , ein supraleiter mit CdI_2 -struktur, *Helv. Phys. Acta* **34**, 408 (1961).
- [42] See Supplemental Material at URL for additional figures, symmetry analysis of the spin-orbit coupling and a single band superconductivity model.
- [43] C. Wang, Y. Xu, and W. Duan, Ising Superconductivity and Its Hidden Variants, *Acc. Mater. Res.* **2**, 526 (2021).
- [44] R. F. Frindt, Superconductivity in ultrathin NbSe_2 layers, *Phys. Rev. Lett.* **28**, 299 (1972).
- [45] S. Nagata, T. Abe, S. Ebisu, Y. Ishihara, and K. Tsutsumi, Superconductivity in the metallic layered compound NbTe_2 , *J. Phys. Chem. Solids* **54**, 895 (1993).
- [46] H. Wang, X. Huang, J. Lin, J. Cui, Y. Chen, C. Zhu, F. Liu, Q. Zeng, J. Zhou, P. Yu, *et al.*, High-quality monolayer superconductor NbSe_2 grown by chemical vapour deposition, *Nat. Commun.* **8**, 1 (2017).
- [47] R. Yan, G. Khalsa, B. T. Schaefer, A. Jarjour, S. Rouvimov, K. C. Nowack, H. G. Xing, and D. Jena, Thickness dependence of superconductivity in ultrathin NbS_2 , *Ap-*

- plied Physics Express **12**, 023008 (2019).
- [48] S. Li, Q. Dong, J. Feng, Y. Wang, M. Hou, W. Deng, R. A. Susilo, N. Li, H. Dong, S. Wan, *et al.*, Evolution of structural and electronic properties in NbTe₂ under high pressure, *Inorg. Chem.* **60**, 7857 (2021).
 - [49] J. Li, P. Song, J. Zhao, K. Vaklinova, X. Zhao, Z. Li, Z. Qiu, Z. Wang, L. Lin, M. Zhao, *et al.*, Printable two-dimensional superconducting monolayers, *Nat. Mater* **20**, 181 (2021).
 - [50] K. Lasek, J. Li, S. Kolekar, P. M. Coelho, L. Guo, M. Zhang, Z. Wang, and M. Batzill, Synthesis and characterization of 2D transition metal dichalcogenides: Recent progress from a vacuum surface science perspective, *Surf. Sci. Rep.* **76**, 100523 (2021).
 - [51] M. Van Maaren and G. Schaeffer, Some new superconducting group va dichalcogenides, *Phys. Lett. A* **24**, 645 (1967).
 - [52] X. Zhang, T. Luo, X. Hu, J. Guo, G. Lin, Y. Li, Y. Liu, X. Li, J. Ge, Y. Xing, *et al.*, Superconductivity and fermi surface anisotropy in transition metal dichalcogenide NbTe₂, *Chin. Phys. Lett* **36**, 1 (2019).
 - [53] Q. Hu, J. Y. Liu, Q. Shi, F. J. Zhang, Y. Zhong, L. Lei, and R. Ang, Charge-density-wave melted superconductivity in 1T-TiSe₂, *EPL* **135**, 57003 (2021).
 - [54] H. Luo, W. Xie, J. Tao, H. Inoue, A. Gyenis, J. W. Krizan, A. Yazdani, Y. Zhu, and R. J. Cava, Polytypism, polymorphism, and superconductivity in TaSe₂-xTex, *PNAS* **112**, E1174 (2015).
 - [55] M. M. May, C. Brabetz, C. Janowitz, and R. Manzke, Charge-density-wave phase of 1T-TiSe₂: The influence of conduction band population, *Phys. Rev. Lett.* **107**, 176405 (2011).
 - [56] N. Giang, Q. Xu, Y. S. Hor, A. J. Williams, S. E. Dutton, H. W. Zandbergen, and R. J. Cava, Superconductivity at 2.3 k in the misfit compound (PbSe)_{1.16}(TiSe₂)₂, *Phys. Rev. B* **82**, 024503 (2010).
 - [57] M. L. Adam, H. Zhu, Z. Liu, S. Cui, P. Zhang, Y. Liu, G. Zhang, X. Wu, Z. Sun, and L. Song, Charge density wave phase suppression in 1T-TiSe₂ through sn intercalation, *Nano Res.* **15**, 2643 (2022).
 - [58] E. Piatti, G. Prando, M. Meinerio, C. Tresca, M. Putti, S. Roddaro, G. Lamura, T. Shiroka, P. Carretta, G. Profeta, D. Daghero, and R. S. Gonnelli, Superconductivity induced by gate-driven hydrogen intercalation in the charge-density-wave compound 1T-TiSe₂, *Commun. Phys.* **6**, 202 (2023).
 - [59] S. Lee, T. B. Park, J. Kim, S.-G. Jung, W. K. Seong, N. Hur, Y. Luo, D. Y. Kim, and T. Park, Tuning the charge density wave quantum critical point and the appearance of superconductivity in Tise₂, *Phys. Rev. Res.* **3**, 033097 (2021).
 - [60] E. Morosan, H. W. Zandbergen, B. S. Dennis, J. W. G. Bos, Y. Onose, T. Klimczuk, A. P. Ramirez, N. P. Ong, and R. J. Cava, Superconductivity in cuxtise₂, *Nat. Phys.* **2**, 544 (2006).
 - [61] E. Morosan, L. Li, N. P. Ong, and R. J. Cava, Anisotropic properties of the layered superconductor cu_{0.07}Tise₂, *Phys. Rev. B* **75**, 104505 (2007).
 - [62] A. F. Kusmartseva, B. Sipos, H. Berger, L. Forró, and E. Tutiš, Pressure induced superconductivity in pristine 1T-TiSe₂, *Phys. Rev. Lett.* **103**, 236401 (2009).
 - [63] R. H. Friend, D. Jerome, and A. D. Yoffe, High-pressure transport properties of TiS₂ and TiSe₂, *J. Phys. C: Solid State Phys.* **15**, 2183 (1982).
 - [64] L. J. Li, E. C. T. O'Farrell, K. P. Loh, G. Eda, B. Özyilmaz, and A. H. Castro Neto, Controlling many-body states by the electric-field effect in a two-dimensional material, *Nature* **529**, 185 (2016).
 - [65] P. Chen, Y.-H. Chan, X.-Y. Fang, Y. Zhang, M. Y. Chou, S.-K. Mo, Z. Hussain, A.-V. Fedorov, and T.-C. Chiang, Charge density wave transition in single-layer titanium diselenide, *Nat. Comm.* **6**, 8943 (2015).
 - [66] P. E. Faria Junior, K. Zollner, T. Woźniak, M. Kurpas, M. Gmitra, and J. Fabian, First-principles insights into the spin-valley physics of strained transition metal dichalcogenides monolayers, *New J. Phys.* **24**, 083004 (2022).
 - [67] S. Raiber, P. E. Faria Junior, D. Falter, S. Feldl, P. Marzena, K. Watanabe, T. Taniguchi, J. Fabian, and C. Schüller, Ultrafast pseudospin quantum beats in multilayer WSe₂ and MoSe₂, *Nat. Commun.* **13**, 4997 (2022).
 - [68] Y. Liu, Z. Wang, X. Zhang, C. Liu, Y. Liu, Z. Zhou, J. Wang, Q. Wang, Y. Liu, C. Xi, M. Tian, H. Liu, J. Feng, X. C. Xie, and J. Wang, Interface-induced zeeman-protected superconductivity in ultrathin crystalline lead films, *Phys. Rev. X* **8**, 021002 (2018).

Supplemental Material: Probing type-II Ising pairing using the spin-mixing parameter

Paulina Jureczko,¹ Jozef Haniš,² Paulo E. Faria Junior,³

Martin Gmitra,^{2,4,*} and Marcin Kurpas^{1,†}

¹*Institute of Physics, University of Silesia in Katowice, 41-500 Chorzów, Poland*

²*Institute of Physics, Pavol Jozef Šafárik University in Košice,
Park Angelinum 9, 04001 Košice, Slovakia*

³*Institute for Theoretical Physics, University of Regensburg, 93040 Regensburg, Germany*

⁴*Institute of Experimental Physics, Slovak Academy of Sciences,
Watsonova 47, 04001 Košice, Slovakia*

I. NON-RELATIVISTIC BAND STRUCTURES

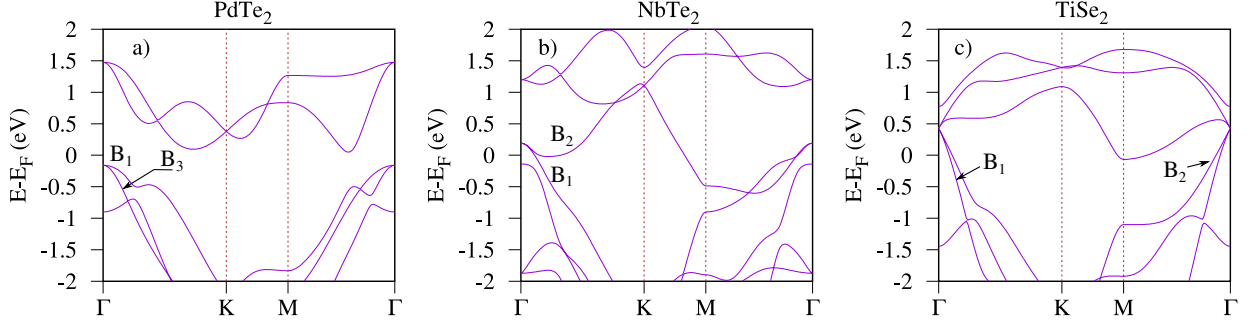


FIG. S1. Non-relativistic band structures of (a) PdTe₂, (b) TiSe₂ and (c) NbTe₂ from first principles.

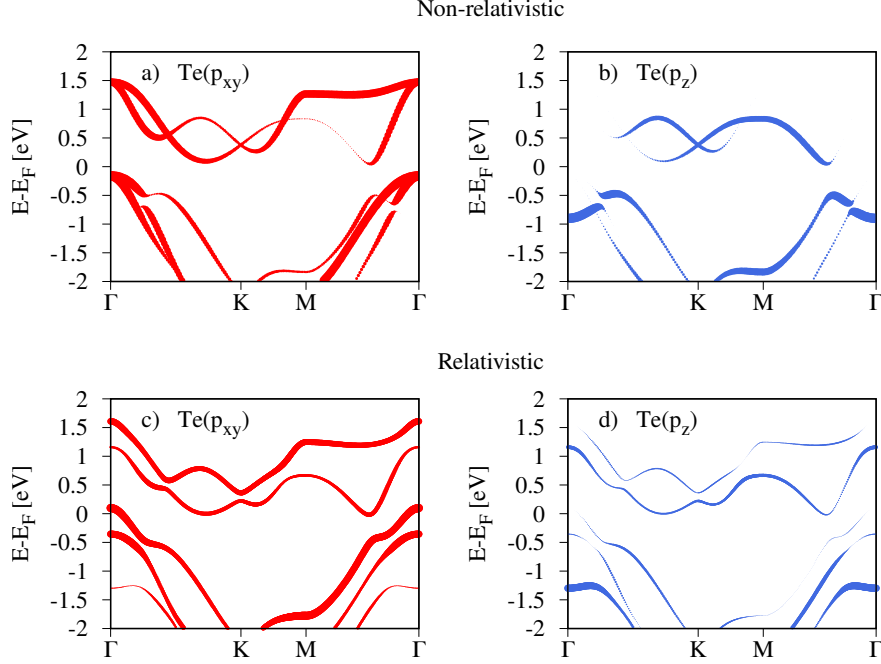


FIG. S2. Non-relativistic (a), (b) and relativistic (c), (d) band structure of PdTe₂ projected on the atomic Te orbitals.

* martin.gmitra@upjs.sk

† marcin.kurpas@us.edu.pl

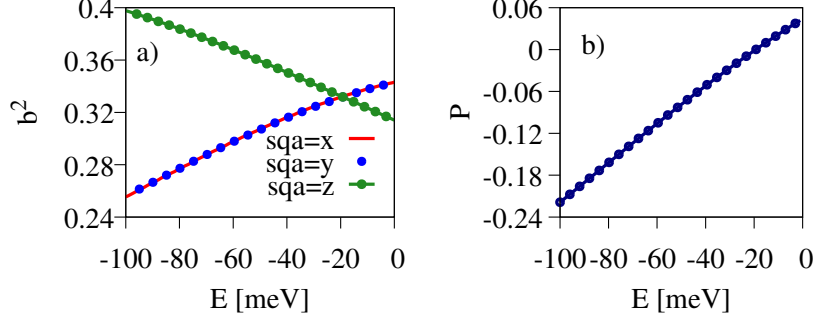


FIG. S3. The average value of (a) the spin-mixing parameter b^2 and (b) polarization P in the band B_3 of PdTe₂, see Fig. S1 (a), in the energy range 100 meV from the top of the band ($E = 0$ eV).

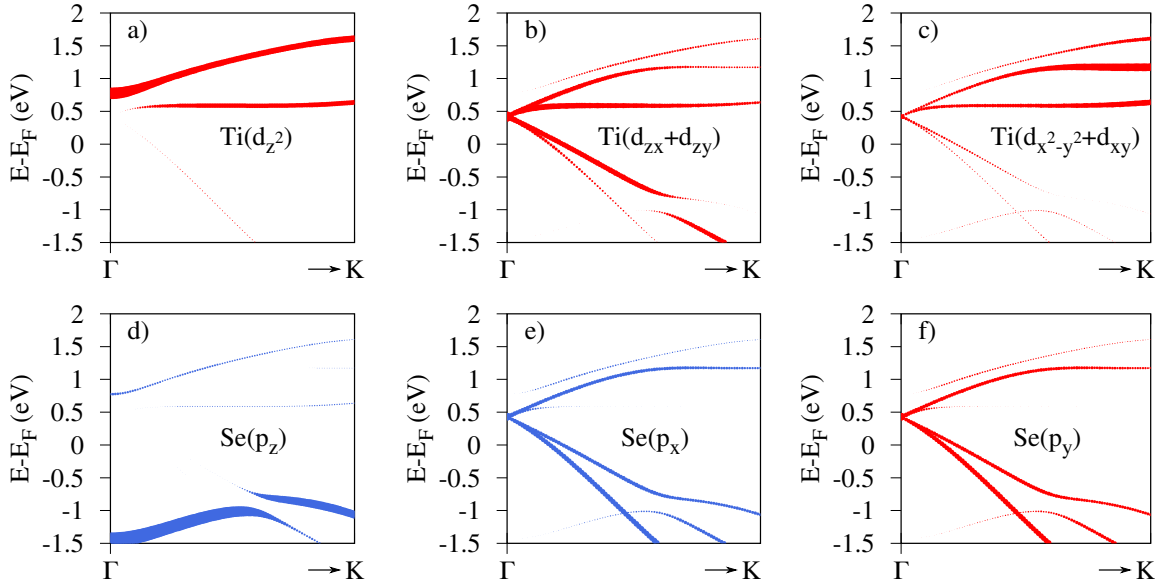


FIG. S4. Non-relativistic band structure of TiSe₂ close to the Γ point projected on the atomic Ti d -orbitals and Se p -orbitals.

II. SYMMETRY ANALYSIS OF Γ -POINT BANDS

The summary of the relevant irreducible representations (irreps) for the energy bands at the Γ -point are given in Fig. S5. Our goal is to perform a symmetry analysis of spin-orbit coupling (SOC) terms to rationalize the calculated b^2 of the relevant bands B1, B2, and B3 (indicated in Fig. 1(b,g,l) in the main text), following the Refs. [1, 2].

All the analyzed materials PdTe₂, NbTe₂, and TiSe₂, have a hexagonal lattice with D_{3d} point-group. The character table of the symmetry group D_{3d} is given in Table I. The nonzero

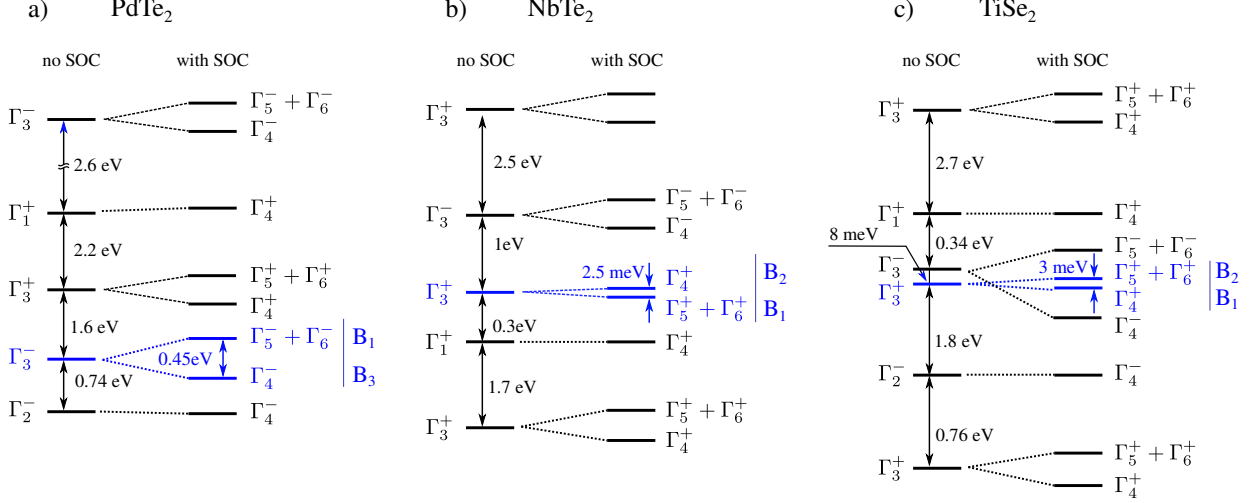


FIG. S5. Irreducible representations (irreps) for Γ -point bands without and with SOC. The irreps in blue indicate the bands B_1 , B_2 , and B_3 presented in Fig. 1(b,g,l) in the main text.

TABLE I. Character table for the group D_{3d} .

D_{3d}	e	$2C_3$	$3C_2'$	i	$2S_6$	$3\sigma_d$	
$\Gamma_1^+ A_{1g}$	1	1	1	1	1	1	$x^2 + y^2, z^2$
$\Gamma_2^+ A_{2g}$	1	1	-1	1	1	-1	R_z
$\Gamma_3^+ E_g$	2	-1	0	2	-1	0	$(R_x, R_y) (x^2 - y^2, xy), (xz, yz)$
$\Gamma_1^- A_{1u}$	1	1	1	-1	-1	-1	
$\Gamma_2^- A_{2u}$	1	1	-1	-1	-1	1	z
$\Gamma_3^- E_u$	2	-1	0	-2	1	0	(x, y)

matrix elements for pseudo-vector operators (R_x, R_y, R_z) can be written as

$$\begin{aligned}
\langle \Gamma_1^+ | R_{x,y} | \Gamma_3^+ \rangle &: \langle \Gamma_1^+ | R_x | \Gamma_{3,1}^+ \rangle = \langle \Gamma_1^+ | R_y | \Gamma_{3,2}^+ \rangle \\
\langle \Gamma_2^+ | R_{x,y} | \Gamma_3^+ \rangle &: \langle \Gamma_2^+ | R_x | \Gamma_{3,2}^+ \rangle = -\langle \Gamma_2^+ | R_y | \Gamma_{3,1}^+ \rangle \\
\langle \Gamma_3^+ | R_{x,y} | \Gamma_3^+ \rangle &: \langle \Gamma_{3,1}^+ | R_x | \Gamma_{3,1}^+ \rangle = -\langle \Gamma_{3,2}^+ | R_x | \Gamma_{3,2}^+ \rangle = -\langle \Gamma_{3,1}^+ | R_y | \Gamma_{3,2}^+ \rangle = -\langle \Gamma_{3,2}^+ | R_y | \Gamma_{3,1}^+ \rangle \\
\langle \Gamma_1^+ | R_z | \Gamma_2^+ \rangle &: \langle \Gamma_1^+ | R_z | \Gamma_2^+ \rangle \\
\langle \Gamma_3^+ | R_z | \Gamma_3^+ \rangle &: \langle \Gamma_{3,1}^+ | R_z | \Gamma_{3,2}^+ \rangle = -\langle \Gamma_{3,2}^+ | R_z | \Gamma_{3,1}^+ \rangle
\end{aligned} \tag{1}$$

$$\begin{aligned}
\langle \Gamma_1^- | R_{x,y} | \Gamma_3^- \rangle &: \langle \Gamma_1^- | R_x | \Gamma_{3,1}^- \rangle = \langle \Gamma_1^- | R_y | \Gamma_{3,2}^- \rangle \\
\langle \Gamma_2^- | R_{x,y} | \Gamma_3^- \rangle &: \langle \Gamma_2^- | R_x | \Gamma_{3,2}^- \rangle = -\langle \Gamma_2^- | R_y | \Gamma_{3,1}^- \rangle \\
\langle \Gamma_3^- | R_{x,y} | \Gamma_3^- \rangle &: \langle \Gamma_{3,1}^- | R_x | \Gamma_{3,1}^- \rangle = -\langle \Gamma_{3,2}^- | R_x | \Gamma_{3,2}^- \rangle = -\langle \Gamma_{3,1}^- | R_y | \Gamma_{3,2}^- \rangle = -\langle \Gamma_{3,2}^- | R_y | \Gamma_{3,1}^- \rangle \\
\langle \Gamma_1^- | R_z | \Gamma_2^- \rangle &: \langle \Gamma_1^- | R_z | \Gamma_2^- \rangle \\
\langle \Gamma_3^- | R_z | \Gamma_3^- \rangle &: \langle \Gamma_{3,1}^- | R_z | \Gamma_{3,2}^- \rangle = -\langle \Gamma_{3,2}^- | R_z | \Gamma_{3,1}^- \rangle
\end{aligned} \tag{2}$$

and, essentially, the same relations connecting the non-zero matrix elements apply for even or odd irreps. Pseudo-vector operators only connect irreps with the same parity.

The SOC term is written as

$$\begin{aligned}
\mathbf{H}_{\text{SO}} &= \frac{\hbar}{4m_0^2c^2} \left(\vec{\nabla} V \times \vec{p} \right) \cdot \vec{\sigma} \\
&= \underbrace{\left[\frac{\hbar}{4m_0^2c^2} \left(\frac{\partial V}{\partial y} p_z - \frac{\partial V}{\partial z} p_y \right) \right]}_{H_{\text{SO}x} \sim R_x} \sigma_x + \underbrace{\left[\frac{\hbar}{4m_0^2c^2} \left(\frac{\partial V}{\partial z} p_x - \frac{\partial V}{\partial x} p_z \right) \right]}_{H_{\text{SO}y} \sim R_y} \sigma_y \\
&\quad + \underbrace{\left[\frac{\hbar}{4m_0^2c^2} \left(\frac{\partial V}{\partial x} p_y - \frac{\partial V}{\partial y} p_x \right) \right]}_{H_{\text{SO}z} \sim R_z} \sigma_z
\end{aligned} \tag{3}$$

The relevant bands of interest, indicated in blue color in Fig. S5, below to Γ_3^- or Γ_3^+ without SOC. Let us focus on the irrep Γ_3^- to investigate the role of intraband and interband SOC. The intraband SOC Hamiltonian for the states $\{ |\Gamma_{3,1}^- \uparrow\rangle, |\Gamma_{3,2}^- \uparrow\rangle, |\Gamma_{3,1}^- \downarrow\rangle, |\Gamma_{3,2}^- \downarrow\rangle \}$ only present a contribution from the $H_{\text{SO}z}$ term since the $H_{\text{SO}x,y}$ terms are forbidden by time-reversal symmetry. The Hamiltonian reads

$$\begin{bmatrix} 0 & i\Delta_z & 0 & 0 \\ -i\Delta_z & 0 & 0 & 0 \\ 0 & 0 & 0 & -i\Delta_z \\ 0 & 0 & i\Delta_z & 0 \end{bmatrix} \tag{4}$$

with $\langle \Gamma_{3,1}^- | H_{\text{SO}z} | \Gamma_{3,2}^- \rangle = -\langle \Gamma_{3,2}^- | H_{\text{SO}z} | \Gamma_{3,1}^- \rangle = i\Delta_z$.

The solutions for this Hamiltonian are given by:

$$\begin{aligned}\Delta_z &\rightarrow |\Gamma_{3-}^- \uparrow\rangle, |\Gamma_{3+}^- \downarrow\rangle \\ -\Delta_z &\rightarrow |\Gamma_{3+}^- \uparrow\rangle, |\Gamma_{3-}^- \downarrow\rangle\end{aligned}\tag{5}$$

with

$$\begin{aligned}|\Gamma_{3\pm}^- \uparrow\rangle &= \frac{1}{\sqrt{2}} (|\Gamma_{3,1}^- \rangle \pm i |\Gamma_{3,2}^- \rangle) |\uparrow\rangle \\ |\Gamma_{3\pm}^- \downarrow\rangle &= \frac{1}{\sqrt{2}} (|\Gamma_{3,1}^- \rangle \pm i |\Gamma_{3,2}^- \rangle) |\downarrow\rangle\end{aligned}\tag{6}$$

The intraband SOC term Δ_z is capable of splitting the energy of opposite spins but does not introduce any spin-mixing. Such spin-mixing arises from the interband SOC. In order to identify the relevant bands that contribute to the spin-mixing and rationalize the magnitude of b^2 at the Γ -point, we evaluate the non-zero corrections to the wave function within 1st order perturbation theory with respect to the \mathbf{H}_{SO} term, i. e.,

$$|\Gamma_{3\alpha}^- \tilde{\sigma}\rangle = |\Gamma_{3\alpha}^- \sigma\rangle + \sum_b^B \frac{\langle b | \mathbf{H}_{\text{SO}} | \Gamma_{3\alpha}^- \sigma \rangle}{E(\Gamma_{3\alpha}^- \sigma) - E(b)} |b\rangle\tag{7}$$

with $\alpha = \pm$, $\sigma = \uparrow, \downarrow \dots$. The \sim indicates the renormalized spin values $\tilde{\sigma} = \uparrow, \downarrow$ after the mixing. The subset B comprises all the other odd irreps present in the system, i.e., $B = \{\Gamma_1^- \oplus \Gamma_2^- \oplus \Gamma_3^-\} \otimes \{\uparrow, \downarrow\}$ (the even irreps are not included since they do not contribute to the coupling, see Eq. (2)). The symmetry analysis allows us to write:

$$\begin{aligned}|\Gamma_{3-}^- \uparrow\rangle &= |\Gamma_{3-}^- \uparrow\rangle + \sum_{\beta}^{\Gamma_3^-} \frac{\langle \beta | H_{\text{SO}z} \sigma_z | \Gamma_{3-}^- \uparrow \rangle}{E(\Gamma_{3-}^- \uparrow) - E(\beta)} |\beta \uparrow\rangle \\ &+ \sum_{\beta}^{\Gamma_1^-, \Gamma_2^-} \frac{\langle \beta \downarrow | H_{\text{SO}x} \sigma_x + H_{\text{SO}y} \sigma_y | \Gamma_{3-}^- \uparrow \rangle}{E(\Gamma_{3-}^- \uparrow) - E(\beta)} |\beta \downarrow\rangle\end{aligned}\tag{8}$$

$$\begin{aligned}
|\Gamma_{3+}^- \downarrow\rangle &= |\Gamma_{3+}^- \downarrow\rangle + \sum_{\beta}^{\Gamma_3^-} \frac{\langle \beta | H_{\text{SO}z} \sigma_z | \Gamma_{3-}^- \downarrow \rangle}{E(\Gamma_{3-}^- \downarrow) - E(\beta)} |\beta \downarrow\rangle \\
&+ \sum_{\beta}^{\Gamma_1^-, \Gamma_2^-} \frac{\langle \beta \uparrow | H_{\text{SO}x} \sigma_x + H_{\text{SO}y} \sigma_y | \Gamma_{3+}^- \downarrow \rangle}{E(\Gamma_{3+}^- \downarrow) - E(\beta)} |\beta \uparrow\rangle
\end{aligned} \tag{9}$$

$$\begin{aligned}
|\Gamma_{3+}^- \uparrow\rangle &= |\Gamma_{3+}^- \uparrow\rangle + \sum_{\beta}^{\Gamma_3^-} \frac{\langle \beta | H_{\text{SO}z} \sigma_z | \Gamma_{3+}^- \uparrow \rangle}{E(\Gamma_{3+}^- \uparrow) - E(\beta)} |\beta \uparrow\rangle \\
&+ \sum_{\beta}^{\Gamma_3^-} \frac{\langle \beta \downarrow | H_{\text{SO}x} \sigma_x + H_{\text{SO}y} \sigma_y | \Gamma_{3+}^- \uparrow \rangle}{E(\Gamma_{3+}^- \uparrow) - E(\beta)} |\beta \downarrow\rangle
\end{aligned} \tag{10}$$

$$\begin{aligned}
|\Gamma_{3-}^- \downarrow\rangle &= |\Gamma_{3-}^- \downarrow\rangle + \sum_{\beta}^{\Gamma_3^-} \frac{\langle \beta | H_{\text{SO}z} \sigma_z | \Gamma_{3-}^- \downarrow \rangle}{E(\Gamma_{3-}^- \downarrow) - E(\beta)} |\beta \downarrow\rangle \\
&+ \sum_{\beta}^{\Gamma_3^-} \frac{\langle \beta \uparrow | H_{\text{SO}x} \sigma_x + H_{\text{SO}y} \sigma_y | \Gamma_{3-}^- \downarrow \rangle}{E(\Gamma_{3-}^- \downarrow) - E(\beta)} |\beta \uparrow\rangle
\end{aligned} \tag{11}$$

And therefore, in summary, we found that:

$$\begin{aligned}
\Delta_z &\rightarrow |\Gamma_{3-}^- \uparrow\rangle, |\Gamma_{3+}^- \downarrow\rangle \rightarrow \text{spin-mixed with } \Gamma_1^-, \Gamma_2^- \text{ bands} \\
-\Delta_z &\rightarrow |\Gamma_{3+}^- \uparrow\rangle, |\Gamma_{3-}^- \downarrow\rangle \rightarrow \text{spin-mixed with } \Gamma_3^- \text{ bands}
\end{aligned} \tag{12}$$

which is also valid for Γ_3^+ bands, which we write down for completeness

$$\begin{aligned}
\Delta_z &\rightarrow |\Gamma_{3-}^+ \uparrow\rangle, |\Gamma_{3+}^+ \downarrow\rangle \rightarrow \text{spin-mixed with } \Gamma_1^+, \Gamma_2^+ \text{ bands} \\
-\Delta_z &\rightarrow |\Gamma_{3+}^+ \uparrow\rangle, |\Gamma_{3-}^+ \downarrow\rangle \rightarrow \text{spin-mixed with } \Gamma_3^+ \text{ bands}
\end{aligned} \tag{13}$$

By inspecting the neighboring bands in Fig. S5, we can make the following statements about b^2 (assuming spin-quantization axis along the z -direction):

- PdTe₂: there is a Γ_2^- band 0.74 eV below the relevant Γ_3^- band and a second Γ_3^- band 6.4 eV above the relevant Γ_3^- band. Therefore, b^2 should be much smaller for $|\Gamma_{3+}^- \uparrow\rangle, |\Gamma_{3-}^- \downarrow\rangle$ than for $|\Gamma_{3-}^- \uparrow\rangle, |\Gamma_{3+}^- \downarrow\rangle$.

- NbTe₂: there is a Γ_1^+ band 0.3 eV below the relevant Γ_3^+ band and two Γ_3^+ bands 3.5 eV above and 2 eV below the relevant Γ_3^+ band. Therefore, b^2 should be smaller for $|\Gamma_{3+}^+ \uparrow\rangle, |\Gamma_{3-}^+ \downarrow\rangle$ than for $|\Gamma_{3-}^+ \uparrow\rangle, |\Gamma_{3+}^+ \downarrow\rangle$.
- TiSe₂: there is a Γ_1^+ band 0.348 eV above the relevant Γ_3^+ band and two Γ_3^+ bands 3.048 eV above and 2.56 eV below the relevant Γ_3^+ band. Therefore, b^2 should be smaller for $|\Gamma_{3+}^+ \uparrow\rangle, |\Gamma_{3-}^+ \downarrow\rangle$ than for $|\Gamma_{3-}^+ \uparrow\rangle, |\Gamma_{3+}^+ \downarrow\rangle$.

This would allow us to identify the double group irreps Γ_4^\pm and $\Gamma_5^\pm \oplus \Gamma_6^\pm$ and the sign of the intraband SOC splitting Δ_z , which we summarize in Table II.

TABLE II. b_z^2 calculated for SQA= z . DG stands for double group and ADG for adapted double group.

		Band	b_z^2	DG irrep	ADG irrep
PdTe ₂	$\Delta_z < 0$	B1	0.000000488	$\Gamma_5^- \oplus \Gamma_6^-$	$ \Gamma_{3+}^- \uparrow\rangle, \Gamma_{3-}^- \downarrow\rangle$
		B3	0.314013252	Γ_4^-	$ \Gamma_{3-}^- \uparrow\rangle, \Gamma_{3+}^- \downarrow\rangle$
NbTe ₂	$\Delta_z > 0$	B1	0.000672534	$\Gamma_5^+ \oplus \Gamma_6^+$	$ \Gamma_{3+}^+ \uparrow\rangle, \Gamma_{3-}^+ \downarrow\rangle$
		B2	0.051897678	Γ_4^+	$ \Gamma_{3-}^+ \uparrow\rangle, \Gamma_{3+}^+ \downarrow\rangle$
TiSe ₂	$\Delta_z < 0$	B1	0.004137026	Γ_4^+	$ \Gamma_{3-}^+ \uparrow\rangle, \Gamma_{3+}^+ \downarrow\rangle$
		B2	0.000038732	$\Gamma_5^+ \oplus \Gamma_6^+$	$ \Gamma_{3+}^+ \uparrow\rangle, \Gamma_{3-}^+ \downarrow\rangle$

III. ESTIMATION OF $B_{c2,\parallel}$

We estimate the temperature dependence of the in-plane upper critical magnetic field $B_{c2,\parallel}$ using the microscopic model for single band superconductivity developed in Ref. [3]:

$$\ln\left(\frac{T}{T_c}\right) + \frac{\mu_B^2 B_{c2,\parallel}}{\widetilde{\beta_{\text{SO}}^2} + \mu_B^2 B_{c2,\parallel}} \text{Re} \left[\psi \left(\frac{1}{2} + \frac{i\sqrt{\beta_{\text{SO}}^2 + \mu_B^2 B_{c2,\parallel}}}{2\pi k_B T} \right) - \psi \left(\frac{1}{2} \right) \right] = 0, \quad (14)$$

where $\widetilde{\beta_{\text{SO}}} = B_\perp / \left(1 + \frac{\hbar}{2\pi k_B T_c \tau_0} \right)$ is the effective Zeeman SOC strength due to the out-of-plane component of the intrinsic SOC field B_\perp , T_c is the critical temperature, μ_B is the Bohr magneton, τ_0 is momentum lifetime, and $\psi(x)$ is the digamma function. The model

was used to extract $B_{c2,\parallel}$ for PdTe₂ from experimental data in Ref. [4]. To provide realistic estimations on $B_{c2,\parallel}$, we use the values of $T_c = 0.7$ K and $\tau_0 = 7.25$ fs extracted from Ref. [4].

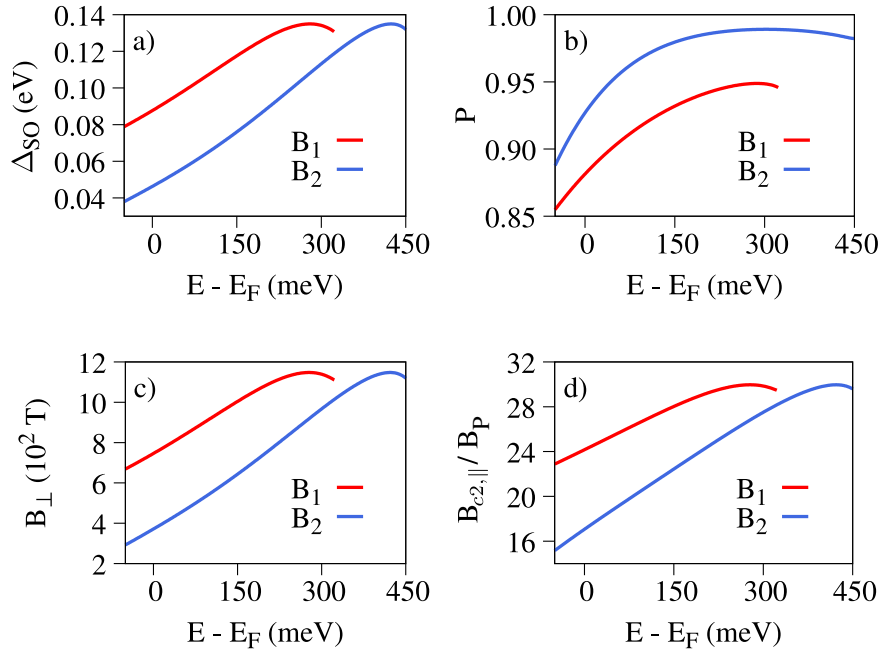


FIG. S6. Calculated average (a) spin-orbital gap Δ_{so} , (b) polarization P , out-of-plane intrinsic SOC field amplitude and (d) in-plane upper critical field $B_{c2,\parallel}(0$ K) for the B_1 and B_2 bands of monolayer TiSe₂ around the Γ point [see Fig. 1 l) in the main text] plotted as a function of the Fermi level varying from -50 meV up to the top of the band at the Γ point. Differences in Δ_{so} and other quantities between the bands B_1 and B_2 come from different energy dispersion (effective masses) of these bands leading to different Fermi contours at a given Fermi energy.

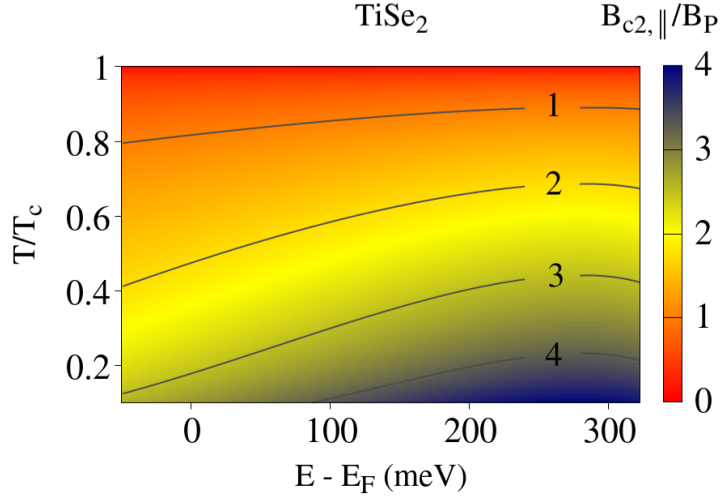


FIG. S7. The upper critical field $B_{c2,||}$ versus temperature and the Fermi level for the band B_1 of TiSe_2 [see Fig. 1 l) in the main text] estimated using Eq. (14).

-
- [1] M. Kurpas, P. E. Faria Junior, M. Gmitra, and J. Fabian, Spin-orbit coupling in elemental two-dimensional materials, *Phys. Rev. B* **100**, 125422 (2019).
 - [2] P. E. Faria Junior, K. Zollner, T. Woźniak, M. Kurpas, M. Gmitra, and J. Fabian, First-principles insights into the spin-valley physics of strained transition metal dichalcogenides monolayers, *New J. Phys.* **24**, 083004 (2022).
 - [3] Y. Liu, Z. Wang, X. Zhang, C. Liu, Y. Liu, Z. Zhou, J. Wang, Q. Wang, Y. Liu, C. Xi, M. Tian, H. Liu, J. Feng, X. C. Xie, and J. Wang, Interface-induced zeeman-protected superconductivity in ultrathin crystalline lead films, *Phys. Rev. X* **8**, 021002 (2018).
 - [4] Y. Liu, Y. Xu, J. Sun, C. Liu, Y. Liu, C. Wang, Z. Zhang, K. Gu, Y. Tang, C. Ding, *et al.*, Type-II Ising Superconductivity and Anomalous Metallic State in Macro-Size Ambient-Stable Ultrathin Crystalline Films, *Nano Lett.* **20**, 5728 (2020).